ACS NANO

ARTICLE

Supramolecular Chirality Synchronization in Thin Films of Plasmonic Nanocomposites

Piotr Szustakiewicz, Natalia Kowalska, Dorota Grzelak, Tetsuya Narushima, Monika Góra, Maciej Bagiński, Damian Pociecha, Hiromi Okamoto, Luis M. Liz-Marzán, and Wiktor Lewandowski*

Read Online

ACCESS | Metrics & More | Article Recommendations | Supporting Information

ABSTRACT: Mirror symmetry breaking in materials is a fascinating phenomenon that has practical implications for various optoelectronic technologies. Chiral plasmonic materials are particularly appealing due to their strong and specific interactions with light. In this work we broaden the portfolio of available strategies toward the preparation of chiral plasmonic assemblies, by applying the principles of chirality synchronization—a phenomenon known for small molecules, which results in the formation of chiral domains from transiently chiral molecules. We report the controlled cocrystallization of 23 nm gold nanoparticles and liquid crystal molecules yielding domains made of highly ordered, helical nanofibers, preferentially twisted to the right or to the left within each domain. We confirmed that such micrometer sized domains exhibit strong, far-field circular dichroism (CD) signals, even though the bulk material is racemic. We further highlight the potential of the proposed approach to realize chiral plasmonic thin films by using a mechanical chirality discrimination method. Toward this end, we developed a rapid CD imaging technique based on the use of polarized light optical microscopy (POM), which enabled probing the CD signal with micrometer-scale resolution, despite of linear dichroism and birefringence in the sample. The developed methodology allows us to extend intrinsically local effects of chiral synchronization to the macroscopic scale, thereby broadening the available tools for chirality manipulation in chiral plasmonic systems.

KEYWORDS: supramolecular chirality, chirality synchronization, nanostructures, dynamic metamaterials, liquid crystals, circular dichroism imaging, helical assemblies
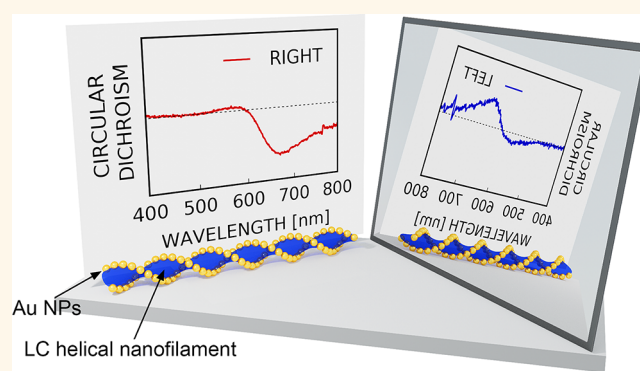
Developing the ability to efficiently manipulate light at will is foreseen as one of the crucial limitations for the emerging technologies of the 21st century. Inspired by nature, scientists and engineers aim at controllably fabricating nanoarchitectures with sophisticated, hierarchical structures, in which the spatial arrangement of building blocks defines the optical response of the material.[1−6] Development of chiral assemblies made of plasmonic nanoparticles is particularly interesting due to their superior light—matter interactions in comparison to purely organic matter.[3,7−12] Stimulated by recent visionary reports, much interest has been revived toward applying the principles of chiral plasmonics to realize super-lenses,[13] chiral catalysts,[14,15] negative refractive index materials,[16] perfect absorbers,[17] broadband circular polarizers,[18] selective reflectors,[19] biosensors,[20] chiral quantum optical devices,[21] chiral emission,[22] and biomanipulation.[23] For this purpose, harnessing chiral plasmonic properties in complex, organic—inorganic nanocomposites is often required. Such composites are usually achieved by either combining intrinsi-

cally chiral NPs[24−27] with achiral materials, through chirality transfer from chiral entities to achiral NPs,[28] or by using other symmetry breaking stimulants, like circularly polarized light[29] or imprinting.[30] The self-assembly driven,[31−34] template-based approach is particularly appealing, as it provides the ability to tailor chiral plasmonic systems. This approach has been realized by tuning the interactions between NPs and chiral DNA,[35,36] peptides,[37,38] proteins,[39] polymers,[40,41] silica,[42] and small molecules[43] used as templates, typically in colloidal or gel systems, and often mimicking the helical geometry of natural materials.[44−46] However, integration of these materials into
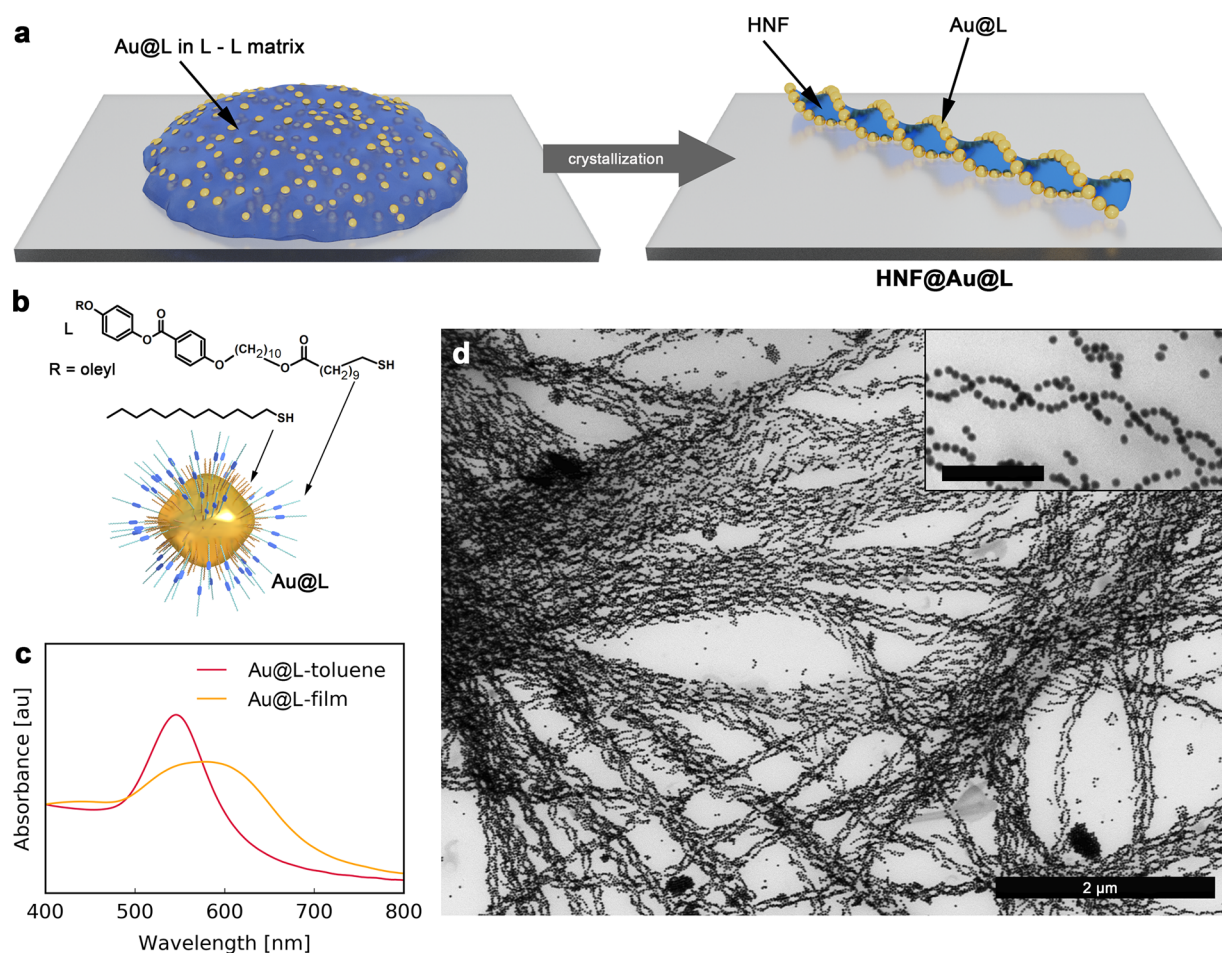
Figure 1. Design and preparation of helical assemblies. (a) Scheme of the formation of Au NPs helical assemblies templated by LCs. (b) Model of L-capped Au quasi-spherical nanoparticles (Au@L) and molecular structure of surface ligands (L and DDT). (c) UV−vis spectra of Au@L dispersion in the toluene and HNF@Au@L films. (d) Representative TEM image of HNF@Au@L; the scale bar in the inset corresponds to 250 nm.

functional devices requires accessible and scalable fabrication methods that rely on inexpensive and readily available constituents. One route to achieve this goal comprises the incorporation of metal nanoparticles within chiral liquid crystal (LC) matrices.[47−50] While yielding materials that exhibit interesting optical properties, this method is limited by the requisite that the organic template must be intrinsically chiral. We propose that achiral constituents can also be used to prepare chiral nanocomposites, which may reduce development costs, if only by broadening the scope of available organic building blocks. In this context, the phenomenon of chirality synchronization in liquid crystal thin films, in which achiral organic molecules break the mirror symmetry by cooperative locking at a given chiral state,[51] seems particularly appealing. One of the most prominent cases of chiral synchronization is related to selected bent-core liquid crystalline compounds[52,53] that are able to form helical nanofilament (HNF) phases.[54,55] At a phase transition into the LC state, nucleation points adopt a certain chiral symmetry, which then propagates through the growth of a domain.[56] The final state is a conglomerate structure made of domains with both left and right handedness. Given the possibility of characterizing homochiral domains using far field methods, as well as the versatility and plasticity of soft,[57−60] thermotropic LC thin films, these materials can be of high technological relevance.[61−65] Recently, some of us demon-

strated the incorporation of metal nanoparticles into HNF materials.[66] However, the principles of chirality synchronization and the resulting optical activity properties are still restricted to the organic-only realm,[51,67−69] thus lacking the advantages of strong light−matter interactions. Although the ability to introduce metal nanoparticles in this kind of material should reinforce the optical properties, up to date only structural asymmetry of NP decorated HNFs has been achieved, with no confirmed plasmonic optical activity.

In this contribution we aimed at achieving plasmonic chiral materials through chirality synchronization in nanocomposites. For this purpose, we used a LC mediated method, which results in helical nanofilaments selectively decorated with gold NPs.[66] Following this methodology, quasi-spherical Au NPs were arranged into a double helical structure. Chirality synchronization enabled the formation of homochiral domains, which was evidenced by far field CD spectroscopy. To enable further manipulation of the materials, a simplified optical microscopy-based method was developed toward the rapid identification of chiral domains by their CD signals, thereby addressing the potential interference from linear effects (linear dichroism, birefringence). CD maps were used to guide the selective removal of homochiral domains (chirality discrimination), leading to nanocomposites exhibiting plasmonic chirality at the bulk scale.
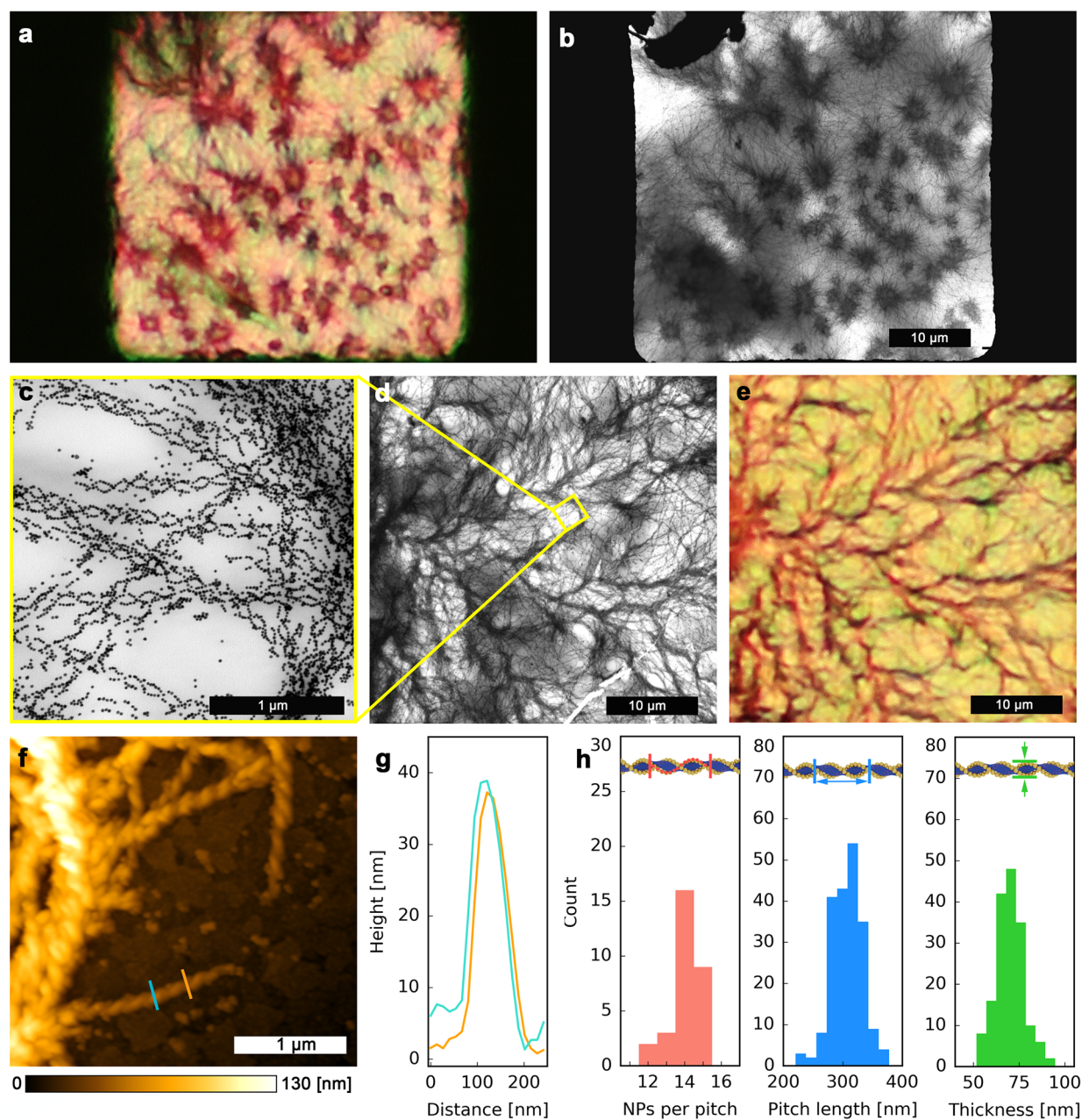
Figure 2. Structural analysis of HNF@Au@L. (a) Optical microscopy image of HNF@Au@L forming multiple domains. Black areas on the sides are parts of the TEM grid mesh. (b) TEM image of the same sample area. (c, d) TEM images showing HNF@Au@L at high and low magnifications, respectively. (e) Optical microscopy image of the same sample area. (f) AFM 2D elevation profile of an edge of an HNF@Au@L domain on an ITO-covered glass substrate. (g) Height profiles from the AFM image shown in panel (f); the colors of the curves correspond to those of the corresponding lines in (f). (h) Structural analysis of HNF@Au@L based on TEM imaging: NPs population per pitch, as well as pitch length and thickness of the helical nanofibers.

RESULTS AND DISCUSSION

Design and Structure of Helical Nanocomposites. In an attempt to prepare thin films exhibiting plasmonic chirality, we used a solid state crystallization method, recently developed by some of us, leading to helical assemblies of NPs.[66] In this method, organic material (L-L) having the ability to form helical nanofilaments is first codispersed with LC-functionalized NPs in toluene, and then the dispersion is dropcasted onto a substrate and heated to reach the isotropic liquid phase. Hierarchical, helical nanocomposites are formed on subsequent cooling (Figure 1a). The underlying mechanism involves a phase transition of the organic compound from isotropic liquid into dendritic, helical filaments, while NPs selectively decorate the edges of such filaments as they are expelled from the bulk L-L phase into the air/fiber boundary.[66] To maximize the efficiency of composite formation we followed a few design principles:

- First, as the organic template material we chose a previously reported L-L dimer (Figure S1).[66] Notably, L-L forms HNFs at a relatively low temperature (110 °C), which prevents heat-induced agglomeration of NPs in the course of composite preparation.

- Second, to achieve a strong plasmonic response from the helical composite in the visible region, we prepared helical assemblies of 23 nm diameter quasi-spherical gold NPs (Figure 1d). The NP size was selected as a compromise between the need to ensure strong plasmonic coupling within the assemblies (which requires larger NPs) and the limited width of the edge in L-L helical nanofilaments (∼30 nm), which are selectively decorated with NPs.

- Finally, efficient formation of helical composites requires the NPs to be well dispersed in the melted organic matrix; thus, chemical compatibility between NPs and the matrix is necessary. Therefore, we incorporated the L ligand (Figure 1b) within the organic shell on the NPs, which was previously shown to ensure compatibility of NPs with the L-L matrix. Using optical microscopy, it was found that an L:DDT (dodecanethiol) molar ratio of 1:1 during the ligand exchange process (which translated to a 1:2 L:DDT ratio found in the NP shell using thermogravimetric analyses, TGA, Figure S2) provides the highest compatibility and allows a uniform dispersion of NPs during the entire heat−cool cycle, whereas a lower proportion of L (1:3 L:DDT during the exchange process), or the exclusive presence of L, were found to result in irreversible NP aggregation during heating (Figure S3). The latter result might suggest that a dense structure of the L shell over the NPs hinders interactions between the ligand and the matrix molecules and thus a lowered density of L grafting is required for efficient miscibility. This can be achieved by means of a mixed organic coating, comprising L and shorter (alkyl) thiols. In this case, we hypothesize that alkyl ligands serve as a spacer and thus create supramolecular pockets for the penetration of matrix molecules; i.e., penetration of the organic shell becomes more efficient, thereby increasing the stability of NP dispersions. However, there is a lower threshold of L content in the shell, below which chemical compatibility between NPs and L-L is not achieved, as evidenced by poor results for the 1:3 L:DDT sample. Similar observations were previously reported for NP composites with LCs[70−73] and polymers.[74] Based on the above, further experiments were carried out using NPs functionalized using 1:1 L:DDT (referred to as Au@L).

As expected, Au@L exhibited a well-defined localized surface plasmon resonance (LSPR) band centered at ∼540 nm in a toluene dispersion (Figure 1c). In a condensed state after the deposition as a thin film, the band was found to broaden and redshift to ∼590 nm (Figure 1c) due to plasmon coupling when the distance (center-to-center) between the neighboring NPs was decreased to ∼26 nm, which roughly translates to 2−3 nm surface-to-surface distance (Figure S4).

To prepare HNF@Au@L, the drop-casted mixtures were quickly (∼40 °C/min) heated up to 140 °C, i.e., ∼30 K above the L-L melting point, to ensure an even dispersion of NPs, as confirmed by optical inspection (Figure S5). In comparison to our previous efforts,[66] an increased temperature was required to achieve well-dispersed NPs, which was likely related to their larger size. The sample was then cooled down to room temperature, at a controlled rate of 40 K/min until reaching 120 °C, and then the rate was reduced to 3 K/min. The first, rapid cooling step was designed to minimize the time NPs are exposed to elevated temperatures, which was not required in our previous contribution.[66] Subsequently, a slower cooling rate was used to stimulate the growth of large domains. Examination by atomic force microscopy (AFM, Figure S6), TEM (Figure 1d, Figure S7), and scanning electron microscopy (SEM, Figure S8) confirmed successful formation of helical nanofilaments decorated with NPs (HNF@Au@L).

One of the key aspects allowing easy and efficient manipulation of HNF@Au@L assemblies is the ability to quickly recognize well-developed helical composites using standard optical microscopy. For this purpose, we compared images obtained by optical and electron microscopies, taken for the same areas of the sample (Figure 2a,b, Figure 2c−e). These images revealed an identical mesoscopic morphology of the sample, confirming the possibility to recognize bundles of HNF@Au@L using an optical microscope. Analysis of TEM images revealed the average pitch of the helical nanostructures to be ∼300 nm, lateral thickness to be ∼68 nm (measured as the distance between centers of Au NPs on opposite sides of the fibers, which translates into ∼44 nm distance between the edges of the organic fibers), and ∼14 particles per pitch for a fully decorated fiber (Figure 2f−h). These structural parameters are comparable to those previously reported for helical nanofilaments formed by liquid crystals.[75] Using AFM, we were able to assess the vertical thickness (height) of a single HNF@Au@L fiber, to be ∼35 nm (Figure 2f−h, Figure S6). The small discrepancy between the values of the lateral thickness and height can be explained by the soft character of the composite, which leads to fibers flattening on the substrate.

Chirality Synchronization Probed with Micro-CD Measurements. Observations of the crystallization process using optical microscopy (Supporting Information Movie 1), as well as optical images of the assemblies (Figure 2a,e, Figure S9, and Figure S10), allowed us to confirm that the growth of HNF@Au@L starts by spontaneous formation of nucleation centers, followed by the dendritic expansion of HNF domains. This growth continues until the isotropic Au@L/L-L melt in contact with the growing domain is completely exhausted. In general, the mechanism of chiral synchronization occurs during the formation of the HNF; i.e., newly added molecules twist in the same direction as the molecules within existing HNF. In our case, Au@L nanoparticles are present within the melt and tend to attach to forming HNFs. This tendency arises from the chemical compatibility (Figure S1) between the L ligand and the L-L matrix. If chiral synchronization occurs independently of the NP deposition on HNFs (in other words, the presence of NPs does not disturb chirality synchronization of L-L), domains with chiral plasmonic response should be formed. Given the achiral environment at the initial stage when nucleation centers are formed, the ratio between left- and right-handed domains is expected to be 1:1, rendering the sample achiral at the bulk scale (racemic). Thus, we decided to perform measurements at the microscale, which should reveal optical activity at the single domain level. For this purpose, we deposited a sample on a glass substrate, allowing for transmission CD measurements with far field, discretely modulated circularly polarized light (DMCPL). In these measurements, one can evaluate directly the difference between extinction (ΔExt) of left and right circularly polarized light (LCP and RCP, respectively),[76,77] thereby enabling CD measurements at the domain scale, despite the strong linear dichroism of HNF@Au@L filaments (Note S1 and Figure S11). The DMCPL approach allows us to eliminate such signal interferences. By using optical microscopy (which provides fast HNF@Au@L domain identification, Figure 2c), a sample area with more than one HNF@Au@L domain was selected (Figure
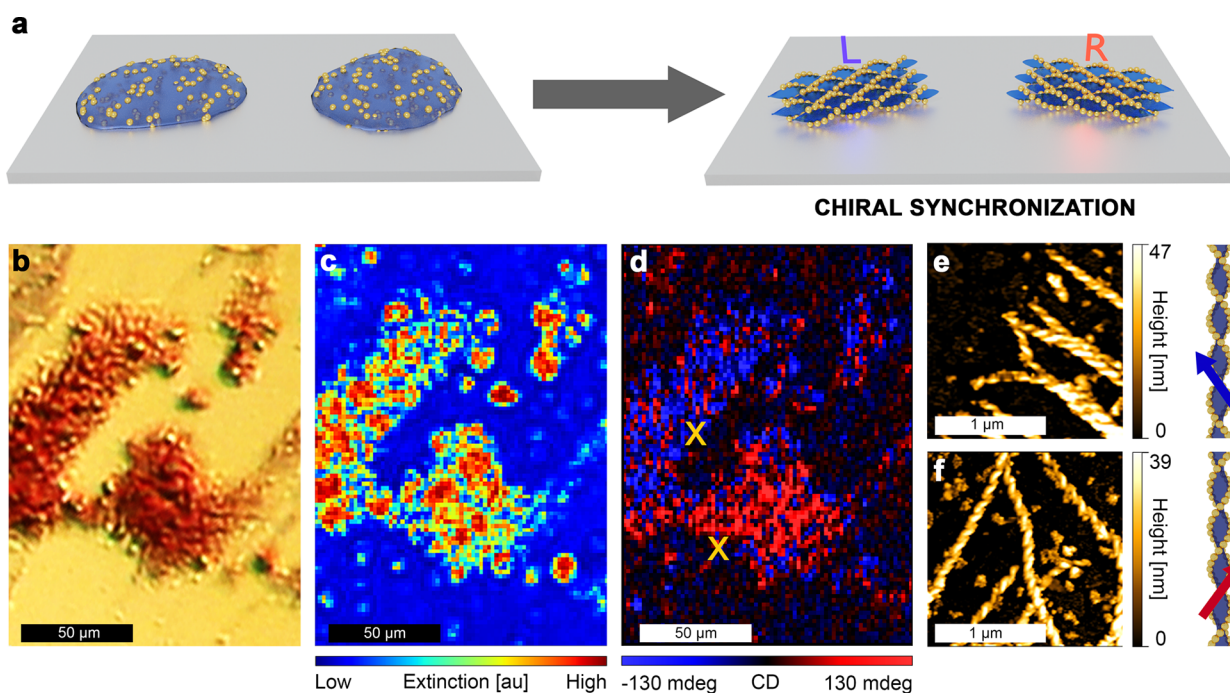
Figure 3. Micrometer-scale circular dichroism measurements. (a) Graphical representation of the chiral synchronization process. (b) Optical micrograph, (c) extinction intensity map at 550 nm, and (d) CD map obtained using a CD microscope with DMCPL at 550 nm from the same region of an HNF@Au@L sample; note that two domains of opposite handedness are revealed. Spatial distribution of CD values is mapped in ellipticity units. (e) AFM height map of a selected region from a left-handed domain (upper X mark in (d) indicates the place of acquisition) and (f) AFM height map of a selected region from a right-handed domain (lower X mark in (d) indicates the place of acquisition). Next to each AFM height map, a graphical model of the helical nanofilament with the corresponding handedness is presented.

3a). First of all, we found that domains can indeed show either negative or positive ΔExt at 550 nm (Figure 3d), confirming the homochirality of particular domains. The 550 nm light was obtained by filtering white light from a supercontinuum laser (EXR-15, NKT Photonics) with a monochromator. At such a light wavelength we were able to isolate the chiral optical response of the nanoparticles from the optical activity of pure organic HNF, which should arise at the UV part of the spectrum (HNF absorbance peaks are below 300 nm, Figure S12), proving that the registered signal originates from plasmonic chirality. It should be noted that domains with the opposite CD signal were undistinguishable when compared by optical microscopy imaging or extinction intensity (Figure 3b,c, respectively), as should be expected if the only difference is the handedness of the HNF. In order to correlate the optical response of the domains with their structure, we performed AFM measurements and found that negative ΔExt was recorded from domains consisting mostly of left-handed HNF (Figure 3e), whereas positive ΔExt originated from domains where right-handed HNFs predominate (Figure 3f). Additional AFM profiles, as well as handedness count analysis, are provided in Figure S13. The observed CD signals are a direct evidence that the helical arrangement, strong plasmonic properties, and relatively short interparticle spacing resulted in chiral plasmonic coupling of NPs. In each domain, small spots (consisting of a few pixels) with opposite handedness were observed. Based on the analysis of the AFM data, most such spots are considered to originate from noise and/or artifacts (Note S2).

Bulk Homochirality via Chirality Discrimination. The results presented so far evidence that single HNF@Au@L domains are optically active. However, to achieve a bulk chiral response some kind of chirality discrimination mechanism

should be applied, leading to an enantiomeric excess of domains with a particular handedness. For this purpose, we devised a simplified measurement technique to probe the plasmonic chirality of micrometer-size domains. The technique is based on a conventional polarization optical microscopy (POM) setup,[78] in which the sample is illuminated by LCP or RCP through installation of a quarter-wave plate (we will refer to the technique as POM-CD, Figure S14 and Note S2). By performing analysis of multiple images for each polarization, we were able to obtain a CD signal map despite of strong linear dichroism of the sample, similar to the case of DMCPL measurements (Figure 3d). The resulting extinction difference map is less accurate and prone to interference (e.g., small changes in the position of the sample during image acquisition would render the results unreliable, Figure S14g,h). However, the time required to obtain data enabling qualitative domain distinction by the CD-signal is much shorter compared to the DMCPL microscopy that we have at present (Note S2).

We then used the technique described above to aid the preparation of thin film samples exhibiting chiral plasmonic properties at a bulk scale. Two samples with HNF@Au@L domains covering a relatively large area (around ~9 mm^2; see Figure S9a for an optical image of one of the samples) were prepared and analyzed with the POM-CD method, using a green filter to restrict the wavelengths to 532 ± 20 nm. We were able to identify the CD-signal of domains with micrometer scale resolution (false color images in Figure 4c,f). We then reduced the population of the domains based on their CD signal through mechanical removal (as demonstrated on Figure 4a): we targeted domains yielding a positive signal in the first sample (Figure 4b−d) and a negative signal in the second one (Figure 4e−g). This proof-of-principle study was performed using a
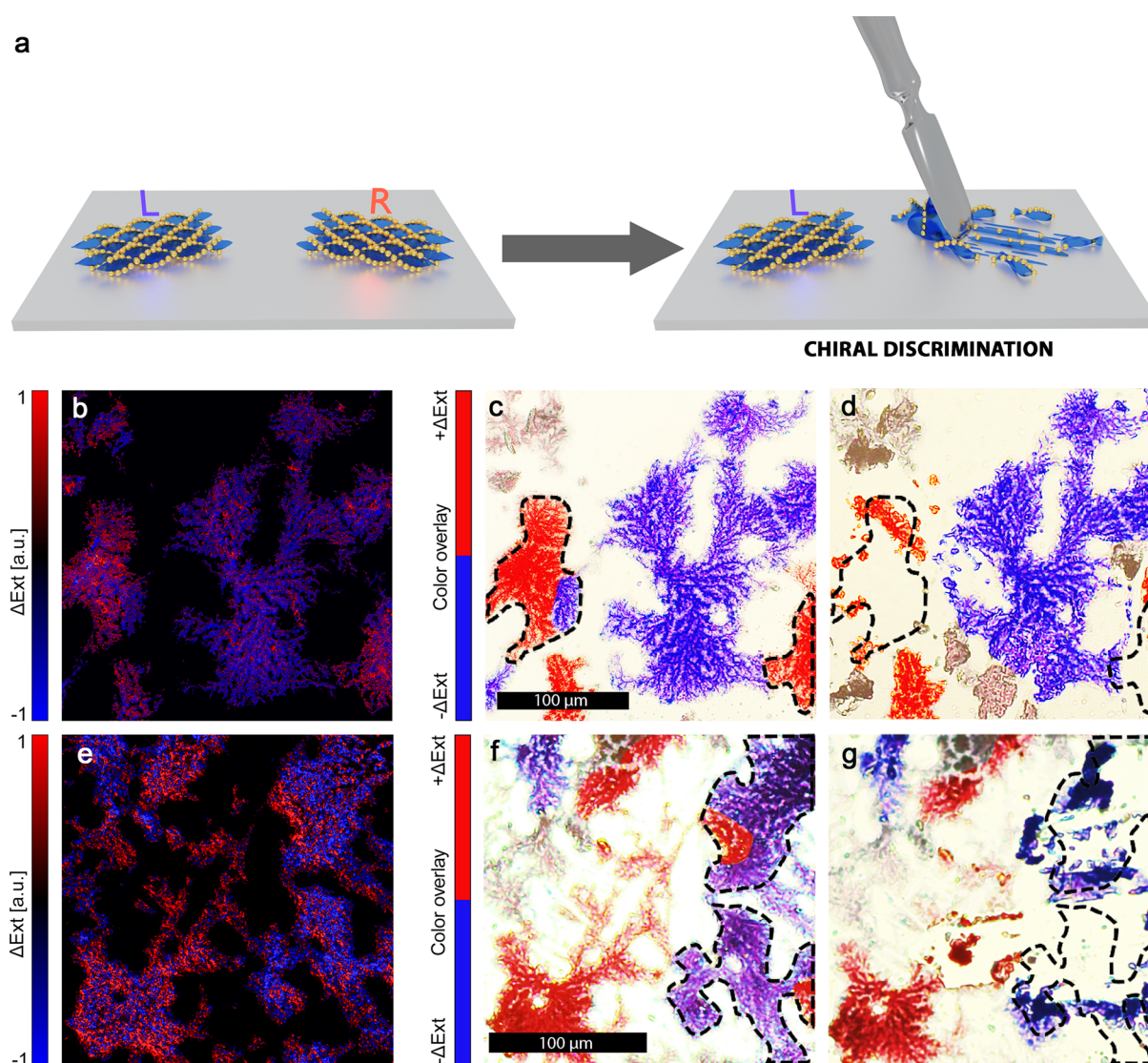
Figure 4. Controlled domain separation. (a) Graphical representation of the chiral discrimination through manual HNF@Au@L removal. (b) ΔExt maps obtained through the POM-CD method, of a HNF@Au@L sample fragment at 532 ± 20 nm. (c) Optical microscopy image of the same region shown in (b) with false-color overlay to highlight domain handedness. (d) Optical microscopy image of the same region shown in (c) after removal of right-handed domains. (e, f, g) Images analogous to those shown in panels (b)−(d) for a sample in which left-handed domains were selectively removed.

simple approach based on optical microscope-assisted, needle-point scratching, which trades precision and scalability for a fast and easy setup with little need for specialized equipment. Due to these limitations, only a certain degree of unbalance between CD positive and negative domains can be introduced, as only relatively large domains (>100 μm diameter) with no opposite-signal neighbors could be targeted.

Both samples were then measured using a commercial CD spectrophotometer, yielding CD signals with a clearly visible Cotton effect around the LSPR absorbance peak—an effect that is typical for strongly absorbing chiral materials[79] and character-istic to NP-decorated helical filaments[80] (Figure 5a). Importantly, changing the orientation of the sample by rotating it along the beam direction axis did not affect the signal (Figure S15). The averaged linear dichroism effect of HNF@Au@L is canceled due to lack of orientational order of filaments on the sample level.

To further confirm that the observed response stems from the chiral arrangement of nanoparticles, we conducted finite difference time-domain (FDTD, Figure 5b) simulations of a helical nanofilament structure made of Au NPs arranged with the average experimentally determined structural parameters (see Materials and Methods for details). The simulated signals are in good agreement with the experimental data, confirming successful preparation of thin film plasmonic structures made of self-assembled helical composites.

CONCLUSIONS

In conclusion, we described a method to obtain chiral plasmonic materials using LC-based self-assembly of gold NPs into helical aggregates. The intense chiral plasmonic response at the microscale is possible because of (1) the intense LSPR and plasmon coupling of relatively large nanoparticles and (2) chiral synchronization—the ability of HNF@Au@L to retain handed-ness during domain growth, resulting in homochiral domains. The high Au filling fraction (~30% mass Au) of the material allows one to observe strong optical properties even for thin film samples.[81] In order to quickly measure CD at a microscale, a
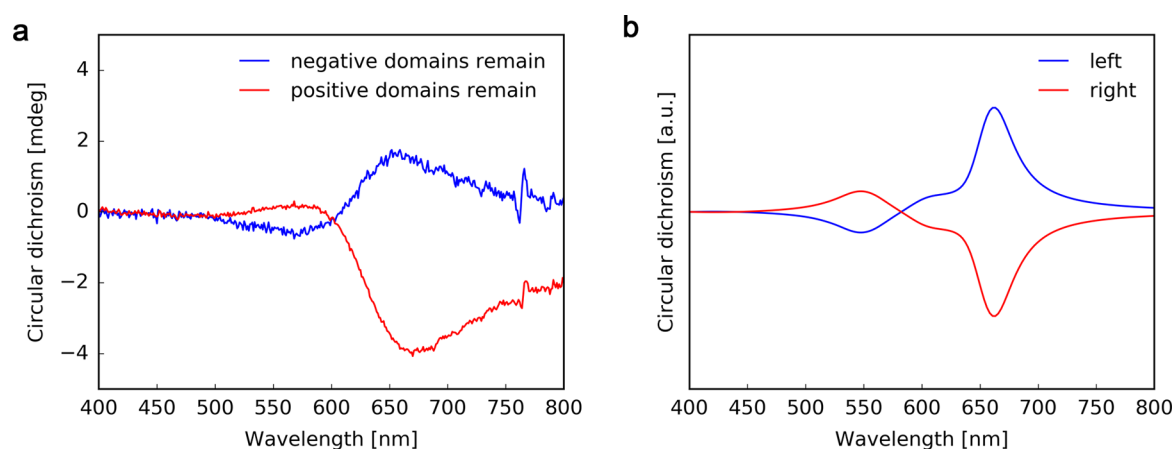
Figure 5. Bulk plasmonic chirality after domain separation. (a) Experimental CD spectra of samples after selective removal of domains with the same handedness. Responses of samples with an excess of right- or left-handed domains are shown in blue and red, respectively. (b) FDTD calculation of the CD spectrum of a single helical nanofilament decorated with 23 nm gold nanoparticles with left- and right-handedness (blue and red, respectively).

simplified, POM-based method for streamlined, qualitative measurements was adapted, which revealed the plasmonic chiral response despite the linear dichroism and birefringence in the thin-film material. This routine allowed us to efficiently map the optical response of large sample areas, which would otherwise be impractical at any larger scale. Being able to quickly determine the CD signal of HNF@Au@L domains, we proposed and successfully demonstrated an efficient approach to obtain plasmonic chirality at a bulk scale, namely, controlled chiral discrimination—a manual removal of either left- or right-handed domains. The approach presented here is a direct evidence that, with the aid of micro-CD measurements, it is possible to translate the chiral synchronization from a local effect at the microscopic scale into a global phenomenon with a bulk-scale optical response, allowing its role in the field of chiral plasmonic materials to be redefined. Utilization of an achiral liquid crystal template ensures low fabrication costs and scalability of the process to maximize the application potential and provides a route toward further reconfigurability.

MATERIALS AND METHODS

Materials. Tetrachloroauric acid (HAuCl$_4$, ≥99%), hexadecyltrimethylammonium chloride (CTAC, 25 wt % in water), benzyldimethylhexadecylammonium chloride (BDAC), citric acid (≥99.5%), sodium borohydride (NaBH$_4$), L-ascorbic acid (AA, ≥99%), tetrahydrofuran (THF, anhydrous, ≥99.9%), dodecanethiol (DDT, ≥98%), and toluene (anhydrous, ≥99.8%) were purchased from Sigma-Aldrich. All chemicals were used without further purification. Milli-Q water was used in all experiments.

Synthesis of Au NPs. Synthesis of Au NPs was carried out according to the seed-mediated growth method reported by Sánchez-Iglesias et al.[82] For the seed preparation, 10 mL of 0.25 mM HAuCl$_4$ solution was reduced by 0.25 mL of freshly prepared 25 mM NaBH$_4$ in the 50 mM CTAC solution, in the presence of citric acid (5 mM) under vigorous stirring. After a few minutes of stirring, the solution was heated at 90 °C under gentle stirring for 90 min. For Au NPs synthesis, 550 μL of seeds was added under vigorous stirring to the growth solution containing 10 mL of 100 mM BDAC, 0.1 mL of 50 mM HAuCl$_4$, and 75 μL of 100 mM AA. The mixture was left undisturbed for 30 min. Before further modifications Au NPs were centrifuged two times (7000 rpm over 15 min) to remove the excess of reactants.

Au NPs Functionalization. The obtained NPs were centrifuged (7000 rpm over 15 min) and redispersed in L−DDT solution in THF in an ultrasonic bath. In a typical process, the molar ratio of Au^0 to L to DDT was 1:1:1. The mixture was left under mild stirring overnight.

Afterward, the excess of ligand was removed through centrifugation. The precipitate containing modified nanoparticles (Au@L) was dispersed in toluene. In the usual procedure a 1:1:1 molar ratio corresponds to 0.1 mg of Au NPs, 0.4 mg of L, and 0.1 mg of DDT.

Synthesis of Organic Materials. L-L and L were synthesized using previously established protocols (Figure S1).[66] Shortly, in the first step, an alkyl spacer unit was synthesized. For this purpose, 11-bromoundecanoic acid was reacted with oxalyl chloride. The formed acid chloride was mixed with 1,12-dodecanediol to obtain an intermediate product (S). Subsequently, ethyl 4-hydroxybenzoate was reacted with an oleyl alcohol in Mitsunobu reaction. Then, a potassium salt of the compound was obtained in a hydrolysis reaction with potassium hydroxide. The salt was then converted to an acid chloride with oxalyl chloride. The acid chloride was subject to an esterification reaction with an excess of hydroquinone. The obtained monoester product was then used as a main substrate for synthesis of L and L-L. To obtain L-L, the Mitsunobu reaction with 1,12-dodecanediol was performed. To obtain L, Mitsunobu reaction with the previously obtained alkyl spacer (S) was conducted. Finally, the bromide atom was substituted with a mercapto group.

HNF@Au@L Sample Preparation. In a typical process, 5 μL of functionalized Au@L toluene solution (2 mg/mL) was added to 5 μL of L-L solution (1 mg/mL) and drop casted on a substrate, usually a TEM grid (~3 μL) or an ITO-covered glass slide (~5 μL). Subsequently, the sample was heated to 140 °C and cooled to 120 °C with a rate ~40 °C/min and then to 30 °C with a precisely controlled rate of 3 °C/min.

FDTD Simulations. Extinction spectra were simulated for HNF@Au@L under LCP and RCP irradiation. HNF parameters were chosen as follows: 14 NPs per pitch, 290 nm pitch length, and 64 nm thickness (measured from center to center of the NPs), which translates into an interparticle separation of ~3.0 nm, in good agreement with the distances measured for the Au@L assemblies. Circular dichroism was calculated as the difference between extinction in RCP and extinction in LCP. The refractive index around the NPs was set to 1.5, as this is a common value for liquid crystal compounds.[83] The perfectly matched layer was set as a boundary condition in all directions. The helical nanofilament direction was perpendicular to incident light. Dielectric functions describing gold were approximated using Johnson and Christy data.[84] All simulations were carried out using Lumerical software.

Methods. For structural analysis of the obtained materials, transmission electron microscopy was used: TEM model JEM-1400 (JEOL, Japan), available at the Nencki Institute of Experimental Biology, laboratory of electron microscopy, and TEM model JEM-1011 (JEOL) equipped with a model EDS INCA analyzer (Oxford, U.K.), in the Electron Microscopy Platform, Massakowski Medical Research Centre, Polish Academy of Science, Warsaw. Scanning electron

microscopy analysis was performed using the Quanta 250, FEG, FEI standard Environmental SEM, available at Wielkopolska Centre For Advanced Technologies. Spectroscopy studies in the UV−vis range were performed using GENESYS 50 UV−vis spectrophotometer, available at the University of Warsaw. In order to determine nanofilament handedness, atomic force microscopy was used. The Bruker Dimension Icon microscope (Billerica, U.S.A.), available at the Biological and Chemical Research Centre, University of Warsaw, was used. The chiral discrimination process was controlled using polarized optical microscopy, Zeiss Axio Imager Am.2 microscope, available at University of Warsaw. Bulk CD measurements were performed using a Chirascan Circular Dichroism Spectrometer, available at University of Warsaw. The cooling−heating process of the obtained samples was controlled using the FTIR600 SP Linkam stage with T96 LinkPad system controller, available at the University of Warsaw. Thermogravimetric measurements were performed using a TGA Q50 by TA Instruments.

ASSOCIATED CONTENT

Ⓢ Supporting Information

The Supporting Information is available free of charge at https://pubs.acs.org/doi/10.1021/acsnano.0c03964.

> Additional figures and notes including linear dichroism, CD imaging microscopy, synthetic routes, thermogravimetric analysis, process optimization, histograms, TEM images, optical microscope images, AFM height map, UV−vis spectrum, 2D AFM elevation profiles, POM-CD method, and circular dichorism spectra (PDF)
>
> Timelapse of HNF@Au@L crystallization (AVI)
>
> Raw micro-CD data (ZIP)

AUTHOR INFORMATION

Corresponding Author

Wiktor Lewandowski − *Laboratory of Organic Nanomaterials and Biomolecules, Faculty of Chemistry, University of Warsaw, 02-093 Warsaw, Poland;* ⓞ orcid.org/0000-0002-3503-2120; Email: wlewandowski@chem.uw.edu.pl

Authors

Piotr Szustakiewicz − *Laboratory of Organic Nanomaterials and Biomolecules, Faculty of Chemistry, University of Warsaw, 02-093 Warsaw, Poland*

Natalia Kowalska − *Laboratory of Organic Nanomaterials and Biomolecules, Faculty of Chemistry, University of Warsaw, 02-093 Warsaw, Poland*

Dorota Grzelak − *Laboratory of Organic Nanomaterials and Biomolecules, Faculty of Chemistry, University of Warsaw, 02-093 Warsaw, Poland*

Tetsuya Narushima − *Institute for Molecular Science (IMS) and The Graduate University for Advanced Studies (SOKENDAI), Okazaki, Aichi 444-8585, Japan*

Monika Góra − *Laboratory of Organic Nanomaterials and Biomolecules, Faculty of Chemistry, University of Warsaw, 02-093 Warsaw, Poland*

Maciej Bagiński − *Laboratory of Organic Nanomaterials and Biomolecules, Faculty of Chemistry, University of Warsaw, 02-093 Warsaw, Poland*

Damian Pociecha − *Faculty of Chemistry, University of Warsaw, 02-089 Warsaw, Poland;* ⓞ orcid.org/0000-0001-7734-3181

Hiromi Okamoto − *Institute for Molecular Science (IMS) and The Graduate University for Advanced Studies (SOKENDAI), Okazaki, Aichi 444-8585, Japan;* ⓞ orcid.org/0000-0003-0082-8652

Luis M. Liz-Marzán − *CIC biomaGUNE, Basque Research and Technology Alliance (BRTA), Donostia-San Sebastián 20014, Spain; Ikerbasque, Basque Foundation for Science, 48013 Bilbao, Spain; Centro de Investigación en Biomédica Red de Bioingeniería, Biomateriales y Nanomedicina (CIBER-BBN), Donostia-San Sebastián 20014, Spain;* ⓞ orcid.org/0000-0002-6647-1353

Complete contact information is available at:
https://pubs.acs.org/10.1021/acsnano.0c03964

Author Contributions

W.L. initiated the project; L.M.L.-M. and W.L. coordinated the work; N.K. performed nanoparticles synthesis, M.B. and M.G. performed organic syntheses; P.S. and N.K. obtained HNF@Au@L and performed TEM, SEM, OM, UV−vis, and bulk-scale CD measurements; W.L. and P.S. performed TGA measurements; D.G. performed AFM measurements; T.N., D.G., and H.O. performed DMCPL measurements; P.S. designed and implemented POM-CD and the chiral discrimination procedure, performed FDTD simulations, and analyzed the data; D.P. helped with optical measurements; P.S. and N.K. prepared the figures; W.L. and P.S. wrote the manuscript draft; and all authors discussed and interpreted the results as well as commented on the manuscript.

Notes

The authors declare no competing financial interest.

REFERENCES

(1) Nitti, A.; Pasini, D. Aggregation-Induced Circularly Polarized Luminescence: Chiral Organic Materials for Emerging Optical Technologies. *Adv. Mater.* **2020**, *32*, 1908021.

(2) Zhao, X.; Zang, S.-Q.; Chen, X. Stereospecific Interactions between Chiral Inorganic Nanomaterials and Biological Systems. *Chem. Soc. Rev.* **2020**, *49*, 2481−2503.

(3) Zhang, L.; Wang, T.; Shen, Z.; Liu, M. Chiral Nanoarchitectonics: Towards the Design, Self-Assembly, and Function of Nanoscale Chiral Twists and Helices. *Adv. Mater.* **2016**, *28*, 1044−1059.

(4) Liu, M.; Zhang, L.; Wang, T. Supramolecular Chirality in Self-Assembled Systems. *Chem. Rev.* **2015**, *115*, 7304−7397.

(5) Wang, L.; Urbas, A. M.; Li, Q. Nature-Inspired Emerging Chiral Liquid Crystal Nanostructures: From Molecular Self-Assembly to DNA Mesophase and Nanocolloids. *Adv. Mater.* **2018**, *32*, 1801335.

(6) Osewski, P.; Belardini, A.; Centini, M.; Valagiannopoulos, C.; Leahu, G.; Li Voti, R.; Tomczyk, M.; Alù, A.; Pawlak, D. A.; Sibilia, C. New Self-Organization Route to Tunable Narrowband Optical Filters and Polarizers Demonstrated with ZnO-ZnWO$_4$ Eutectic Composite. *Adv. Opt. Mater.* **2020**, *8*, 1901617.

(7) Lan, X.; Wang, Q. Self-Assembly of Chiral Plasmonic Nanostructures. *Adv. Mater.* **2016**, *28*, 10499−10507.

(8) Hentschel, M.; Schäferling, M.; Duan, X.; Giessen, H.; Liu, N. Chiral Plasmonics. *Sci. Adv.* **2017**, *3*, No. e1602735.

(9) Olesiak-Banska, J.; Waszkielewicz, M.; Obstarczyk, P.; Samoc, M. Two-Photon Absorption and Photoluminescence of Colloidal Gold Nanoparticles and Nanoclusters. *Chem. Soc. Rev.* **2019**, *48*, 4087−4117.

(10) Guerrero-Martínez, A.; Alonso-Gómez, J. L.; Auguié, B.; Cid, M. M.; Liz-Marzán, L. M. From Individual to Collective Chirality in Metal Nanoparticles. *Nano Today* **2011**, *6*, 381−400.

(11) Kumar, J.; Thomas, K. G.; Liz-Marzán, L. M. Nanoscale Chirality in Metal and Semiconductor Nanoparticles. *Chem. Commun.* **2016**, *52*, 12555−12569.

(12) Mosquera, J.; Zhao, Y.; Jang, H. J.; Xie, N.; Xu, C.; Kotov, N. A.; Liz-Marzán, L. M. Plasmonic Nanoparticles with Supramolecular Recognition. *Adv. Funct. Mater.* **2020**, *30*, 1902082.

(13) Zhang, S.; Park, Y. S.; Li, J.; Lu, X.; Zhang, W.; Zhang, X. Negative Refractive Index in Chiral Metamaterials. *Phys. Rev. Lett.* **2009**, *102*, 023901.

(14) Khorashad, L. K.; Besteiro, L. V.; Correa-Duarte, M. A.; Burger, S.; Wang, Z. M.; Govorov, A. O. Hot Electrons Generated in Chiral Plasmonic Nanocrystals as a Mechanism for Surface Photochemistry and Chiral Growth. *J. Am. Chem. Soc.* **2020**, *142*, 4193−4305.

(15) He, C.; Feng, Z.; Shan, S.; Wang, M.; Chen, X.; Zou, G. Highly Enantioselective Photo-Polymerization Enhanced by Chiral Nanoparticles and *In Situ* Photopatterning of Chirality. *Nat. Commun.* **2020**, *11*, 1188.

(16) Panpradit, W.; Sonsilphong, A.; Soemphol, C.; Wongkasem, N. High Negative Refractive Index in Chiral Metamaterials. *J. Opt.* **2012**, *14*, 075101.

(17) Wang, W.; Besteiro, L. V.; Liu, T.; Wu, C.; Sun, J.; Yu, P.; Chang, L.; Wang, Z.; Govorov, A. O. Generation of Hot Electrons with Chiral Metamaterial Perfect Absorbers: Giant Optical Chirality for Polarization-Sensitive Photochemistry. *ACS Photonics* **2019**, *6*, 3241−3252.

(18) Gansel, J. K.; Thiel, M.; Rill, M. S.; Decker, M.; Bade, K.; Saile, V.; Von Freymann, G.; Linden, S.; Wegener, M. Gold Helix Photonic Metamaterial as Broadband Circular Polarizer. *Science* **2009**, *325*, 1513−1515.

(19) Qiu, M.; Zhang, L.; Tang, Z.; Jin, W.; Qiu, C. W.; Lei, D. Y. 3D Metaphotonic Nanostructures with Intrinsic Chirality. *Adv. Funct. Mater.* **2018**, *28*, 1803147.

(20) Solomon, M. L.; Saleh, A. A. E.; Poulikakos, L. V.; Abendroth, J. M.; Tadesse, L. F.; Dionne, J. A. Nanophotonic Platforms for Chiral Sensing and Separation. *Acc. Chem. Res.* **2020**, *53*, 588−598.

(21) Vanacore, G. M.; Berruto, G.; Madan, I.; Pomarico, E.; Biagioni, P.; Lamb, R. J.; McGrouther, D.; Reinhardt, O.; Kaminer, I.; Barwick, B.; Larocque, H.; Grillo, V.; Karimi, E.; García de Abajo, F. J.; Carbone, F. Ultrafast Generation and Control of an Electron Vortex Beam *via* Chiral Plasmonic near Fields. *Nat. Mater.* **2019**, *18*, 573−579.

(22) Zhao, B.; Yu, H.; Pan, K.; Tan, Z.; Deng, J. Multifarious Chiral Nanoarchitectures Serving as Handed-Selective Fluorescence Filters for Generating Full-Color Circularly Polarized Luminescence. *ACS Nano* **2020**, *14*, 3208−3218.

(23) Zhao, X.; Xu, L.; Sun, M.; Ma, W.; Wu, X.; Xu, C.; Kuang, H. Tuning the Interactions between Chiral Plasmonic Films and Living Cells. *Nat. Commun.* **2017**, *8*, 2007.

(24) Luo, J.; Cheng, Y.; Gong, Z. W.; Wu, K.; Zhou, Y.; Chen, H. X.; Gauthier, M.; Cheng, Y. Z.; Liang, J.; Zou, T. Self-Assembled Peptide

Functionalized Gold Nanopolyhedrons with Excellent Chiral Optical Properties. *Langmuir* **2020**, *36*, 600−608.

(25) Lee, H. E.; Kim, R. M.; Ahn, H. Y.; Lee, Y. Y.; Byun, G. H.; Im, S. W.; Mun, J.; Rho, J.; Nam, K. T. Cysteine-Encoded Chirality Evolution in Plasmonic Rhombic Dodecahedral Gold Nanoparticles. *Nat. Commun.* **2020**, *11*, 263.

(26) Lee, H.-E.; Ahn, H.-Y.; Mun, J.; Lee, Y. Y.; Kim, M.; Cho, N. H.; Chang, K.; Kim, W. S.; Rho, J.; Nam, K. T. Amino-Acid- and Peptide-Directed Synthesis of Chiral Plasmonic Gold Nanoparticles. *Nature* **2018**, *556*, 360−365.

(27) González-Rubio, G.; Mosquera, J.; Kumar, V.; Pedrazo-Tardajos, A.; Llombart, P.; Solís, D. M.; Lobato, I.; Noya, E. G.; Guerrero-Martínez, A.; Taboada, J. M.; Obelleiro, F.; MacDowell, L. G.; Bals, S.; Liz-Marzán, L. M. Micelle-Directed Chiral Seeded Growth on Anisotropic Gold Nanocrystals. *Science* **2020**, *368*, 1472−1477.

(28) Morrow, S. M.; Bissette, A. J.; Fletcher, S. P. Transmission of Chirality through Space and across Length Scales. *Nat. Nanotechnol.* **2017**, *12*, 410−419.

(29) Kim, J.-Y.; Yeom, J.; Zhao, G.; Calcaterra, H.; Munn, J.; Zhang, P.; Kotov, N. Assembly of Gold Nanoparticles into Chiral Superstructures Driven by Circularly Polarized Light. *J. Am. Chem. Soc.* **2019**, *141*, 11739−11744.

(30) Zhang, M.; Pacheco-Peña, V.; Yu, Y.; Chen, W.; Greybush, N. J.; Stein, A.; Engheta, N.; Murray, C. B.; Kagan, C. R. Nanoimprinted Chiral Plasmonic Substrates with Three-Dimensional Nanostructures. *Nano Lett.* **2018**, *18*, 7389−7394.

(31) Urban, M. J.; Shen, C.; Kong, X.-T.; Zhu, C.; Govorov, A. O.; Wang, Q.; Hentschel, M.; Liu, N. Chiral Plasmonic Nanostructures Enabled by Bottom-Up Approaches. *Annu. Rev. Phys. Chem.* **2019**, *70*, 275−299.

(32) Hsu, S. W.; Rodarte, A. L.; Som, M.; Arya, G.; Tao, A. R. Colloidal Plasmonic Nanocomposites: From Fabrication to Optical Function. *Chem. Rev.* **2018**, *118*, 3100−3120.

(33) Xu, W.; Li, Z.; Yin, Y. Colloidal Assembly Approaches to Micro/Nanostructures of Complex Morphologies. *Small* **2018**, *14*, 1801083.

(34) Schreiber, R.; Luong, N.; Fan, Z.; Kuzyk, A.; Nickels, P. C.; Zhang, T.; Smith, D. M.; Yurke, B.; Kuang, W.; Govorov, A. O.; Liedl, T. Chiral Plasmonic DNA Nanostructures with Switchable Circular Dichroism. *Nat. Commun.* **2013**, *4*, 2948.

(35) Kuzyk, A.; Schreiber, R.; Fan, Z.; Pardatscher, G.; Roller, E.-M.; Högele, A.; Simmel, F. C.; Govorov, A. O.; Liedl, T. DNA-Based Self-Assembly of Chiral Plasmonic Nanostructures with Tailored Optical Response. *Nature* **2012**, *483*, 311−314.

(36) Golla, M.; Albert, S. K.; Atchimnaidu, S.; Perumal, D.; Krishnan, N.; Varghese, R. DNA-Decorated, Helically Twisted Nanoribbons: A Scaffold for the Fabrication of One-Dimensional, Chiral, Plasmonic Nanostructures. *Angew. Chem., Int. Ed.* **2019**, *58*, 3865−3869.

(37) Nakagawa, M.; Kawai, T. Chirality-Controlled Syntheses of Double-Helical Au Nanowires. *J. Am. Chem. Soc.* **2018**, *140*, 4991−4994.

(38) Lu, J.; Chang, Y. X.; Zhang, N. N.; Wei, Y.; Li, A. J.; Tai, J.; Xue, Y.; Wang, Z. Y.; Yang, Y.; Zhao, L.; Lu, Z.; Liu, K. Chiral Plasmonic Nanochains *via* the Self-Assembly of Gold Nanorods and Helical Glutathione Oligomers Facilitated by Cetyltrimethylammonium Bromide Micelles. *ACS Nano* **2017**, *11*, 3463−3475.

(39) Zhang, Q.; Hernandez, T.; Smith, K. W.; Hosseini Jebeli, S. A.; Dai, A. X.; Warning, L.; Baiyasi, R.; McCarthy, L. A.; Guo, H.; Chen, D.-H.; Dionne, J. A.; Landes, C. F.; Link, S. Unraveling the Origin of Chirality from Plasmonic Nanoparticle-Protein Complexes. *Science* **2019**, *365*, 1475−1478.

(40) Abdilla, A.; Dolinski, N. D.; De Roos, P.; Ren, J. M.; Van Der Woude, E.; Seo, S. E.; Zayas, M. S.; Lawrence, J.; Read De Alaniz, J.; Hawker, C. J. Polymer Stereocomplexation as a Scalable Platform for Nanoparticle Assembly. *J. Am. Chem. Soc.* **2020**, *142*, 1667−1672.

(41) Li, L.; Zhang, Y.; Lu, H.; Wang, Y.; Xu, J.; Zhu, J.; Zhang, C.; Liu, T. Cryopolymerization Enables Anisotropic Polyaniline Hybrid Hydrogels with Superelasticity and Highly Deformation-Tolerant Electrochemical Energy Storage. *Nat. Commun.* **2020**, *11*, 62.

(42) Gao, J.; Wu, W.; Lemaire, V.; Carvalho, A.; Nlate, S.; Buffeteau, T.; Oda, R.; Battie, Y.; Pauly, M.; Pouget, E. Tuning the Chiroptical Properties of Elongated Nano-Objects *via* Hierarchical Organization. *ACS Nano* **2020**, *14*, 4111−4121.

(43) Guerrero-Martínez, A.; Auguié, B.; Alonso-Gómez, J. L.; Džolić, Z.; Gómez-Graña, S.; Žinić, M.; Cid, M. M.; Liz-Marzán, L. M. Intense Optical Activity from Three-Dimensional Chiral Ordering of Plasmonic Nanoantennas. *Angew. Chem., Int. Ed.* **2011**, *50*, 5499−5503.

(44) Passaseo, A.; Esposito, M.; Cuscunà, M.; Tasco, V. Materials and 3D Designs of Helix Nanostructures for Chirality at Optical Frequencies. *Adv. Opt. Mater.* **2017**, *5*, 1601079.

(45) Zhou, Y.; Marson, R. L.; Van Anders, G.; Zhu, J.; Ma, G.; Ercius, P.; Sun, K.; Yeom, B.; Glotzer, S. C.; Kotov, N. A. Biomimetic Hierarchical Assembly of Helical Supraparticles from Chiral Nanoparticles. *ACS Nano* **2016**, *10*, 3248−3256.

(46) Kaschke, J.; Wegener, M. Optical and Infrared Helical Metamaterials. *Nanophotonics* **2016**, *5*, 510−523.

(47) Mori, T.; Sharma, A.; Hegmann, T. Significant Enhancement of the Chiral Correlation Length in Nematic Liquid Crystals by Gold Nanoparticle Surfaces Featuring Axially Chiral Binaphthyl Ligands. *ACS Nano* **2016**, *10*, 1552−1564.

(48) Querejeta-Fernández, A.; Kopera, B.; Prado, K. S.; Klinkova, A.; Methot, M.; Chauve, G.; Bouchard, J.; Helmy, A. S.; Kumacheva, E. Circular Dichroism of Chiral Nematic Films of Cellulose Nanocrystals Loaded with Plasmonic Nanoparticles. *ACS Nano* **2015**, *9*, 10377−10385.

(49) Li, Z.; Liu, H.; Li, F.; Zhao, J.; Wang, Y. Self-Assembly of Chiral Nematic Liquid Crystalline Phases of AgNR@SiO$_2$@Cysteine@ CsPbBr$_3$ Hybrid Nanorods with Plasmon-Dependent Photoluminescence. *Part. Part. Syst. Charact.* **2020**, *37*, 2000008.

(50) Nemati, A.; Shadpour, S.; Querciagrossa, L.; Mori, T.; Zannoni, C.; Hegmann, T. Highly Sensitive, Tunable Chirality Amplification through Space Visualized for Gold Nanorods Capped with Axially Chiral Binaphthyl Derivatives. *ACS Nano* **2019**, *13*, 10312−10326.

(51) Chang, B.; Li, X.; Sun, T. Self-Assembled Chiral Materials from Achiral Components or Racemates. *Eur. Polym. J.* **2019**, *118*, 365−381.

(52) Le, K. V.; Takezoe, H.; Araoka, F. Chiral Superstructure Mesophases of Achiral Bent-Shaped Molecules - Hierarchical Chirality Amplification and Physical Properties. *Adv. Mater.* **2017**, *29*, 1602737.

(53) Stevenson, W. D.; Zeng, X.; Welch, C.; Thakur, A. K.; Ungar, G.; Mehl, G. H. Macroscopic Chirality of Twist-Bend Nematic Phase in Bent Dimers Confirmed by Circular Dichroism. *J. Mater. Chem. C* **2020**, *8*, 1041−1047.

(54) Hough, L. E.; Jung, H. T.; Krüerke, D.; Heberling, M. S.; Nakata, M.; Jones, C. D.; Chen, D.; Link, D. R.; Zasadzinski, J.; Heppke, G.; Rabe, J. P.; Stocker, W.; Körblova, E.; Walba, D. M.; Glaser, M. A.; Clark, N. A. Helical Nanofilament Phases. *Science* **2009**, *325*, 456−460.

(55) Zhang, C.; Diorio, N.; Lavrentovich, O. D.; Jákli, A. Helical Nanofilaments of Bent-Core Liquid Crystals with a Second Twist. *Nat. Commun.* **2014**, *5*, 3302.

(56) Chen, D.; Tuchband, M. R.; Horanyi, B.; Korblova, E.; Walba, D. M.; Glaser, M. A.; Maclennan, J. E.; Clark, N. A. Diastereomeric Liquid Crystal Domains at the Mesoscale. *Nat. Commun.* **2015**, *6*, 7763.

(57) Kim, H.; Ryu, S. H.; Tuchband, M.; Shin, T. J.; Korblova, E.; Walba, D. M.; Clark, N. A.; Yoon, D. K. Structural Transitions and Guest/Host Complexing of Liquid Crystal Helical Nanofilaments Induced by Nanoconfinement. *Sci. Adv.* **2017**, *3*, No. e1602102.

(58) Shadpour, S.; Nemati, A.; Liu, J.; Hegmann, T. Directing the Handedness of Helical Nanofilaments Confined in Nanochannels Using Axially Chiral Binaphthyl Dopants. *ACS Appl. Mater. Interfaces* **2020**, *12*, 13456−13463.

(59) Park, W.; Ha, T.; Kim, T.-T.; Zep, A.; Ahn, H.; Shin, T. J.; Sim, K. I.; Jung, T. S.; Kim, J. H.; Pociecha, D.; Górecka, E.; Yoon, D. K. Directed Self-Assembly of a Helical Nanofilament Liquid Crystal Phase for Use as Structural Color Reflectors. *NPG Asia Mater.* **2019**, *11*, 45.

(60) Kim, H.; Lee, S.; Shin, T. J.; Cha, Y. J.; Korblova, E.; Walba, D. M.; Clark, N. A.; Lee, S. B.; Yoon, D. K. Alignment of Helical Nanofilaments on the Surfaces of Various Self-Assembled Monolayers. *Soft Matter* **2013**, *9*, 6185−6191.

(61) Kim, Y.; Yeom, B.; Arteaga, O.; Jo Yoo, S.; Lee, S.-G.; Kim, J.-G.; Kotov, N. A. Reconfigurable Chiroptical Nanocomposites with Chirality Transfer from the Macro- to the Nanoscale. *Nat. Mater.* **2016**, *15*, 461−468.

(62) Guo, J.; Kim, J.; Zhang, M.; Wang, H.; Stein, A.; Murray, C. B.; Kotov, N. A.; Kagan, C. R. Chemo- and Thermomechanically Configurable 3D Optical Metamaterials Constructed from Colloidal Nanocrystal Assemblies. *ACS Nano* **2020**, *14*, 1427−1435.

(63) Jin, X.; Jiang, J.; Liu, M. Reversible Plasmonic Circular Dichroism *via* Hybrid Supramolecular Gelation of Achiral Gold Nanorods. *ACS Nano* **2016**, *10*, 11179−11186.

(64) Wang, M.; Dong, J.; Zhou, C.; Xie, H.; Ni, W.; Wang, S.; Jin, H.; Wang, Q. Reconfigurable Plasmonic Diastereomers Assembled by DNA Origami. *ACS Nano* **2019**, *13*, 13702−13708.

(65) Kowerdziej, R.; Wróbel, J.; Kula, P. Ultrafast Electrical Switching of Nanostructured Metadevice with Dual-Frequency Liquid Crystal. *Sci. Rep.* **2019**, *9*, 20367.

(66) Bagiński, M.; Tupikowska, M.; González-Rubio, G.; Wójcik, M.; Lewandowski, W. Shaping Liquid Crystals with Gold Nanoparticles: Helical Assemblies with Tunable and Hierarchical Structures *via* Thin-Film Cooperative Interactions. *Adv. Mater.* **2020**, *32*, 1904581.

(67) Buchs, J.; Vogel, L.; Janietz, D.; Prehm, M.; Tschierske, C. Chirality Synchronization of Hydrogen-Bonded Complexes of Achiral N-Heterocycles. *Angew. Chem., Int. Ed.* **2017**, *56*, 280−284.

(68) Park, W.; Wolska, J. M.; Pociecha, D.; Gorecka, E.; Yoon, D. K. Direct Visualization of Optical Activity in Chiral Substances Using a Helical Nanofilament (B4) Liquid Crystal Phase. *Adv. Opt. Mater.* **2019**, *7*, 1901399.

(69) Lehmann, A.; Alaasar, M.; Poppe, M.; Poppe, S.; Prehm, M.; Nagaraj, M.; Sreenilayam, S. P.; Panarin, Y. P.; Vij, J. K.; Tschierske, C. Stereochemical Rules Govern the Soft Self-Assembly of Achiral Compounds: Understanding the Heliconical Liquid-Crystalline Phases of Bent-Core Mesogens. *Chem. - Eur. J.* **2020**, *26*, 4714−4733.

(70) Milette, J.; Toader, V.; Reven, L.; Lennox, R. B. Tuning the Miscibility of Gold Nanoparticles Dispersed in Liquid Crystals *via* the Thiol-for-DMAP Reaction. *J. Mater. Chem.* **2011**, *21*, 9043.

(71) Milette, J.; Toader, V.; Soulé, E. R.; Lennox, R. B.; Rey, A. D.; Reven, L. A Molecular and Thermodynamic View of the Assembly of Gold Nanoparticles in Nematic Liquid Crystal. *Langmuir* **2013**, *29*, 1258−1263.

(72) Qi, H.; Kinkead, B.; Marx, V. M.; Zhang, H. R.; Hegmann, T. Miscibility and Alignment Effects of Mixed Monolayer Cyanobiphenyl Liquid-Crystal-Capped Gold Nanoparticles in Nematic Cyanobiphenyl Liquid Crystal Hosts. *ChemPhysChem* **2009**, *10*, 1211−1218.

(73) Gharbi, M. A.; Manet, S.; Lhermitte, J.; Brown, S.; Milette, J.; Toader, V.; Sutton, M.; Reven, L. Reversible Nanoparticle Cubic Lattices in Blue Phase Liquid Crystals. *ACS Nano* **2016**, *10*, 3410−3415.

(74) Martin, T. B.; Dodd, P. M.; Jayaraman, A. Polydispersity for Tuning the Potential of Mean Force between Polymer Grafted Nanoparticles in a Polymer Matrix. *Phys. Rev. Lett.* **2013**, *110*, 018301.

(75) Kim, H.; Ryu, S. H.; Tuchband, M.; Shin, T. J.; Korblova, E.; Walba, D. M.; Clark, N. A.; Yoon, D. K. Structural Transitions and Guest/Host Complexing of Liquid Crystal Helical Nanofilaments Induced by Nanoconfinement. *Sci. Adv.* **2017**, *3*, No. e1602102.

(76) Narushima, T.; Okamoto, H. Circular Dichroism Microscopy Free from Commingling Linear Dichroism *via* Discretely Modulated Circular Polarization. *Sci. Rep.* **2016**, *6*, 35731.

(77) Yamada, T.; Eguchi, T.; Wakiyama, T.; Narushima, T.; Okamoto, H.; Kimizuka, N. Synthesis of Chiral Labtb and Visualization of Its Enantiomeric Excess by Induced Circular Dichroism Imaging. *Chem. - Eur. J.* **2019**, *25*, 6698−6702.

(78) Claborn, K.; Puklin-Faucher, E.; Kurimoto, M.; Kaminsky, W.; Kahr, B. Circular Dichroism Imaging Microscopy: Application to Enantiomorphous Twinning in Biaxial Crystals of 1,8-Dihydroxyanthraquinone. *J. Am. Chem. Soc.* **2003**, *125*, 14825−14831.

(79) Ma, W.; Kuang, H.; Wang, L.; Xu, L.; Chang, W. S.; Zhang, H.; Sun, M.; Zhu, Y.; Zhao, Y.; Liu, L.; Xu, C.; Link, S.; Kotov, N. A. Chiral Plasmonics of Self-Assembled Nanorod Dimers. *Sci. Rep.* **2013**, *3*, 1934.

(80) Song, C.; Blaber, M. G.; Zhao, G.; Zhang, P.; Fry, H. C.; Schatz, G. C.; Rosi, N. L. Tailorable Plasmonic Circular Dichroism Properties of Helical Nanoparticle Superstructures. *Nano Lett.* **2013**, *13*, 3256−3261.

(81) Young, K. L.; Ross, M. B.; Blaber, M. G.; Rycenga, M.; Jones, M. R.; Zhang, C.; Senesi, A. J.; Lee, B.; Schatz, G. C.; Mirkin, C. A. Using DNA to Design Plasmonic Metamaterials with Tunable Optical Properties. *Adv. Mater.* **2014**, *26*, 653−659.

(82) Sánchez-Iglesias, A.; Winckelmans, N.; Altantzis, T.; Bals, S.; Grzelczak, M.; Liz-Marzán, L. M. High-Yield Seeded Growth of Monodisperse Pentatwinned Gold Nanoparticles through Thermally Induced Seed Twinning. *J. Am. Chem. Soc.* **2017**, *139*, 107−110.

(83) Li, J.; Wen, C. H.; Gauza, S.; Lu, R.; Wu, S. T. Refractive Indices of Liquid Crystals for Display Applications. *J. Disp. Technol.* **2005**, *1*, 51−61.

(84) Johnson, P. B.; Christy, R. W. Optical Constatnts for Noble Metals. *Phys. Rev. B* **1972**, *6*, 4370.